JSC manuscript No.
(will be inserted by the editor)

Efficient Absorbing Layers for Weakly Compressible Flows

Z. Gao · J.S. Hesthaven · T. Warburton

Received: date / Accepted: date

Abstract Seeking to develop efficient and accurate absorbing layers for the low-speed weakly compressible Navier-Stokes equations, we exploit the connection to the BGK-approximation to develop an absorbing layer with qualities similar to that of the perfectly matched layer (PML) known from linear wave problems. Representing the solutions to the BGK approximation as variations from the Maxwellian distribution allows for a direct connection to the compressible Navier-Stokes equation while leading to a linear system of equations with nonlinearities expressed in low order terms only. This allows for a direct construction of an absorbing layer with PML-like properties.

We demonstrate the accuracy of the BGK approximation and the efficiency of the absorbing layer for the BGK model before pursuing this as a

Z. Gao
Key Laboratory of Marine Environment & Ecology, Ministry of Education, and School of Mathematical Sciences, Ocean University of China, Qingdao, 266100, China
E-mail: zhengao@ouc.edu.cn

J.S. Hesthaven
Division of Applied Mathematics, Brown University, Providence, RI 02912, USA
E-mail: Jan.Hesthaven@brown.edu

T. Warburton
Department of Computational and Applied Mathematics, Rice University, Houston, 77005, USA
E-mail: tim.warburton@gmail.com

means of truncating the full Navier-Stokes equations with a flux based coupling between the different regions. Examples including sound propagation and vortex shedding confirms the accuracy of the approach. Although we focus on two-dimensional isentropic examples, the development generalizes to the three-dimensional non-isentropic case.

Keywords Navier-Stokes equations, BGK model, perfectly matched layer, absorbing layer

1 Introduction

In this paper, we take a path different from most previous work and first consider the BGK approximation as a model for weakly compressible flows. Discretizing this in a special way results in a linear hyperbolic problem with all nonlinearities in low order terms only. After having qualitatively validated the accuracy of this model, we develop a PML for the homogeneous part of this approximation and show that this is both accurate and efficient as an absorbing layer for both acoustic and vortical flows. The close connection to the full compressible Navier-Stokes equations then suggests that an efficient absorbing layer is possible by terminating the Navier-Stokes equations with a layer in which the absorbing layer BGK model is solved. It is this hybrid, involving a combination of both model approximations and results from absorbing layers for linear problems, that is the main contribution in this work and, as we shall demonstrate through a variety of test cases, offers interesting perspectives for the development of efficient and accurate absorbing layers of the fully nonlinear compressible Navier-Stokes equations.

What remains of the paper is organized as follows. In Sec. 2 we recall the two-dimensional isentropic Navier-Stokes equations while Sec. 3 discusses the BGK model, its approximation and reduction to a linear system, and the connection to Navier-Stokes equations. We also demonstrate the surprising accuracy of the model for bounded problems. Sec. 4 develops the perfectly matched layer for the BGK approximation, offers some insight into the properties of the model and discusses the accuracy and general behavior for a few

test cases. That sets the stage for Sec. 5 in which we propose to combine an internal full Navier-Stokes equation model with the BGK-related absorbing layer as a way to effectively truncate unsteady problems of weakly compressible gas dynamics. After having demonstrated the accuracy of this approach, we conclude in Sec. 6 with a few remarks and an outlook.

2 The compressible Navier-Stokes equations

We discuss the development and evaluation of efficient absorbing layers for the two-dimensional Navier-Stokes equations for a compressible isentropic gas described by

$$\frac{\partial \rho}{\partial t} + \frac{\partial \rho u}{\partial x_1} + \frac{\partial \rho v}{\partial x_2} = 0, \tag{1}$$

$$\frac{\partial \rho u}{\partial t} + \frac{\partial (\rho u^2 + p)}{\partial x_1} + \frac{\partial \rho uv}{\partial x_2} = \frac{\partial \sigma_{11}}{\partial x_1} + \frac{\partial \sigma_{12}}{\partial x_2},$$

$$\frac{\partial \rho v}{\partial t} + \frac{\partial \rho uv}{\partial x_1} + \frac{\partial (\rho v^2 + p)}{\partial x_2} = \frac{\partial \sigma_{21}}{\partial x_1} + \frac{\partial \sigma_{22}}{\partial x_2},$$

where $\boldsymbol{x} = (x_1, x_2) \in \mathbb{D}$ represent the spatial domain, ρ is the density, ρu and ρv are the x_1- and x_2-components of the momentum, p is the internal pressure, related to the density through the ideal gas law, $p = \mathbb{R}\mathbb{T}\rho$. Here $\mathbb{R}$ is the gas constant and $\mathbb{T}$ the thermodynamic temperature. The stress tensor, σ, is assumed to be of the form

$$\begin{aligned}
\sigma_{11} &= \nu \left(2\tfrac{\partial u}{\partial x_1} - \tfrac{2}{3} \left(\tfrac{\partial u}{\partial x_1} + \tfrac{\partial v}{\partial x_2} \right) \right), \\
\sigma_{12} = \sigma_{21} &= \nu \left(\tfrac{\partial u}{\partial x_2} + \tfrac{\partial v}{\partial x_1} \right), \\
\sigma_{22} &= \nu \left(2\tfrac{\partial v}{\partial x_2} - \tfrac{2}{3} \left(\tfrac{\partial u}{\partial x_1} + \tfrac{\partial v}{\partial x_2} \right) \right).
\end{aligned}$$

where ν is the kinematic viscosity. We assume throughout that the kinematic viscosity is independent of density and is homogeneous in space.

At solid boundaries, the no-slip boundary condition is imposed by $\rho u = \rho v = 0$ while the density is determined by the internal state. This choice is consistent with classic analysis of well posed boundary conditions [1].

3 The BGK model and its approximation

The BGK approximation [2] of the Boltzmann equation is given as

$$\frac{\partial f}{\partial t} + \boldsymbol{\zeta} \cdot \nabla_x f = -\frac{1}{\gamma}(f - f_{\mathrm{B}}(\rho, \boldsymbol{u})). \tag{2}$$

Here $f(t, \boldsymbol{\zeta}, \boldsymbol{x})$ is the particle distribution function, $\boldsymbol{\zeta} = (\zeta_1, \zeta_2, \zeta_3)$ is the microscopic velocity and γ represents the relaxation time, i.e., the right hand side models the collisions while the left hand side of the equation accounts for transport and mixing.

The Maxwell-Boltzmann equilibrium distribution function $f_{\mathrm{B}}(\rho, \boldsymbol{u})$ is given as

$$f_{\mathrm{B}}(\rho, \boldsymbol{u}) = \frac{\rho}{(2\pi\mathbb{RT})^{d/2}} \exp\left(-\frac{|\boldsymbol{\zeta} - \boldsymbol{u}|^2}{2\mathbb{RT}}\right), \tag{3}$$

where d is the dimension of space.

The relation between $f(t, \boldsymbol{\zeta}, \boldsymbol{x})$ and the macroscopic flow properties, density ρ, the momentum $\rho\boldsymbol{u}$, and the pressure tensor $\mathbb{P}_{\alpha\beta}$, are given as [3]

$$\rho = \int_{-\infty}^{+\infty} f \, d\boldsymbol{\zeta}, \qquad \rho u_\alpha = \int_{-\infty}^{+\infty} \zeta_\alpha f \, d\boldsymbol{\zeta}, \qquad \mathbb{P}_{\alpha\beta} = \int_{-\infty}^{+\infty} (\zeta_\alpha - u_\alpha)(\zeta_\beta - u_\beta) f \, d\boldsymbol{\zeta}. \tag{4}$$

The stresses $\sigma_{\alpha\beta}$ is defined by

$$\sigma_{\alpha\beta} = \mathbb{I}p - \mathbb{P}_{\alpha\beta}, \tag{5}$$

where $p = \frac{1}{3}\mathrm{tr}\{\mathbb{P}_{\alpha\beta}\} = \mathbb{RT}\rho$ is the scalar pressure.

3.1 Approximating the approximation

Solving the BGK-model directly is clearly a challenge, given its 6+1 dimensional nature and attempting to do so will overwhelm all cost of solving the compressible Navier-Stokes equations. We shall therefore seek an approximation and given the essentially unbounded velocity space, it is perhaps natural to seek an expansion in Hermite polynomials as

$$f(t,\boldsymbol{\zeta},\boldsymbol{x}) = \sum_{k=0}^{\infty} a_k(\boldsymbol{x},t)\xi_k(\boldsymbol{\zeta}),$$

where ξ_k is a properly enumerated basis expressed by Hermite polynomials.

We recall that Hermite polynomials, see e.g. [4], are orthogonal polynomials defined on $[-\infty,+\infty]$ satisfying

$$\int_{-\infty}^{+\infty} \exp(-\frac{x^2}{2})\mathbb{H}_i(x)\mathbb{H}_j(x)dx = \delta_{ij}\sqrt{2\pi}, \tag{6}$$

with

$$\mathbb{H}_0(x) = 1, \quad \mathbb{H}_1(x) = x, \quad \mathbb{H}_2(x) = \frac{x^2-1}{\sqrt{2}}, \quad \mathbb{H}_3(x) = \cdots .$$

However, since we are primarily interested in considering perturbations around the equilibrium distribution, it is natural to consider a slightly modified approximation, first proposed in [5]

$$f(t,\mathbf{x},\zeta) = \frac{\rho}{(2\pi\mathbb{RT})^{d/2}} \exp\left(-\frac{\boldsymbol{\zeta}\cdot\boldsymbol{\zeta}}{2\mathbb{RT}}\right) \sum_{k=0}^{\infty} a_k(\boldsymbol{x},t)\xi_k(\boldsymbol{\zeta}). \tag{7}$$

An immediate consequence of this is that one recovers the Maxwellian distribution for $k = 0$.

We shall use this ansatz up to second order Hermite polynomials as the basis - a basis that has the following elements

$$\begin{aligned}
\xi_0 &= \mathbb{H}_0(\tfrac{\zeta_1}{\sqrt{\mathbb{RT}}})\mathbb{H}_0(\tfrac{\zeta_2}{\sqrt{\mathbb{RT}}}) = 1,\\
\xi_1 &= \mathbb{H}_1(\tfrac{\zeta_1}{\sqrt{\mathbb{RT}}})\mathbb{H}_0(\tfrac{\zeta_2}{\sqrt{\mathbb{RT}}}) = \tfrac{\zeta_1}{\sqrt{\mathbb{RT}}},\\
\xi_2 &= \mathbb{H}_0(\tfrac{\zeta_1}{\sqrt{\mathbb{RT}}})\mathbb{H}_1(\tfrac{\zeta_2}{\sqrt{\mathbb{RT}}}) = \tfrac{\zeta_2}{\sqrt{\mathbb{RT}}},\\
\xi_3 &= \mathbb{H}_1(\tfrac{\zeta_1}{\sqrt{\mathbb{RT}}})\mathbb{H}_1(\tfrac{\zeta_2}{\sqrt{\mathbb{RT}}}) = \tfrac{\zeta_1\zeta_2}{\mathbb{RT}},\\
\xi_4 &= \mathbb{H}_2(\tfrac{\zeta_1}{\sqrt{\mathbb{RT}}})\mathbb{H}_0(\tfrac{\zeta_2}{\sqrt{\mathbb{RT}}}) = \tfrac{1}{\sqrt{2}}(\tfrac{\zeta_1^2}{\mathbb{RT}} - 1),\\
\xi_5 &= \mathbb{H}_0(\tfrac{\zeta_1}{\sqrt{\mathbb{RT}}})\mathbb{H}_2(\tfrac{\zeta_2}{\sqrt{\mathbb{RT}}}) = \tfrac{1}{\sqrt{2}}(\tfrac{\zeta_2^2}{\mathbb{RT}} - 1),
\end{aligned} \tag{8}$$

where we, for simplicity only, have restricted it to the two-dimensional case with $\boldsymbol{\zeta} = (\zeta_1, \zeta_2)$.

Substituting (7) into (2), one obtains

$$\mathbb{R}(a_0,\cdots,a_5,\boldsymbol{\zeta}) = \frac{\partial f}{\partial t} + \boldsymbol{\zeta}\cdot\nabla_x f + \frac{f - f_{\mathrm{B}}(a_0,a_1,a_2)}{\gamma}. \tag{9}$$

Employing a Galerkin procedure, we recover

$$\begin{array}{l}
\frac{\partial a_0}{\partial t} + \sqrt{\mathbb{RT}}(\frac{\partial a_1}{\partial x_1} + \frac{\partial a_2}{\partial x_2}) = 0, \\
\frac{\partial a_1}{\partial t} + \sqrt{\mathbb{RT}}(\frac{\partial a_0}{\partial x_1} + \sqrt{2}\frac{\partial a_4}{\partial x_1} + \frac{\partial a_3}{\partial x_2}) = 0, \\
\frac{\partial a_2}{\partial t} + \sqrt{\mathbb{RT}}(\frac{\partial a_3}{\partial x_1} + \frac{\partial a_0}{\partial x_2} + \sqrt{2}\frac{\partial a_5}{\partial x_2}) = 0, \\
\frac{\partial a_3}{\partial t} + \sqrt{\mathbb{RT}}(\frac{\partial a_2}{\partial x_1} + \frac{\partial a_1}{\partial x_2}) = -\frac{1}{\gamma}(a_3 - \frac{a_1 a_2}{a_0}), \\
\frac{\partial a_4}{\partial t} + \sqrt{2\mathbb{RT}}\frac{\partial a_1}{\partial x_1} = -\frac{1}{\gamma}(a_4 - \frac{a_1^2}{\sqrt{2}a_0}), \\
\frac{\partial a_5}{\partial t} + \sqrt{2\mathbb{RT}}\frac{\partial a_2}{\partial x_2} = -\frac{1}{\gamma}(a_5 - \frac{a_2^2}{\sqrt{2}a_0}).
\end{array} \tag{10}$$

For clarity, let us write this system as

$$\frac{\partial \boldsymbol{a}}{\partial t} + \sum_i A_1 \frac{\partial \boldsymbol{a}}{\partial x_i} = S(\boldsymbol{a}), \tag{11}$$

where $\boldsymbol{a} = (a_0, \cdots, a_5)^T$ and

$$A_1 = \sqrt{\mathbb{RT}} \begin{pmatrix} 0 & 1 & 0 & 0 & 0 & 0 \\ 1 & 0 & 0 & 0 & \sqrt{2} & 0 \\ 0 & 0 & 0 & 1 & 0 & 0 \\ 0 & 0 & 1 & 0 & 0 & 0 \\ 0 & \sqrt{2} & 0 & 0 & 0 & 0 \\ 0 & 0 & 0 & 0 & 0 & 0 \end{pmatrix}, \quad A_2 = \sqrt{\mathbb{RT}} \begin{pmatrix} 0 & 0 & 1 & 0 & 0 & 0 \\ 0 & 0 & 0 & 1 & 0 & 0 \\ 1 & 0 & 0 & 0 & 0 & \sqrt{2} \\ 0 & 1 & 0 & 0 & 0 & 0 \\ 0 & 0 & 0 & 0 & 0 & 0 \\ 0 & 0 & \sqrt{2} & 0 & 0 & 0 \end{pmatrix}, \tag{12}$$

and $S(\boldsymbol{a})$ is a nonlinear source with the elements

$$S(\bar{a}) = -\frac{1}{\gamma}\left(0, 0, 0, a_3 - \frac{a_1 a_2}{a_0}, a_4 - \frac{a_1^2}{\sqrt{2}a_0}, a_5 - \frac{a_2^2}{\sqrt{2}a_0}\right)^T.$$

It is straightforward to see that the above system is symmetric hyperbolic following standard definitions, see e.g. [5].

Utilizing the thermodynamic connection to the macroscopic quantities in (4-5) and the properties of the Hermite polynomials, one immediately recovers the connection between the expansion coefficients, a_k, and the macroscopic quantities as

$$
\begin{aligned}
\rho &= \int_{-\infty}^{+\infty} f_{\mathrm{B}}\, d\boldsymbol{\zeta} = a_0, \\
u &= \int_{-\infty}^{+\infty} \zeta_1 f_{\mathrm{B}}\, d\boldsymbol{\zeta} = \tfrac{a_1\sqrt{\mathbb{R}\mathbb{T}}}{a_0}, \quad v = \int_{-\infty}^{+\infty} \zeta_2 f_{\mathrm{B}}\, d\boldsymbol{\zeta} = \tfrac{a_2\sqrt{\mathbb{R}\mathbb{T}}}{a_0}, \\
\sigma_{11} &= -\int_{-\infty}^{+\infty} (\zeta_1 - u)^2 f_{\mathrm{B}}\, d\boldsymbol{\zeta} + \mathbb{R}\mathbb{T}\rho = -\mathbb{R}\mathbb{T}(\sqrt{2}a_4 - \tfrac{a_1^2}{a_0}), \\
\sigma_{22} &= -\int_{-\infty}^{+\infty} (\zeta_2 - v)^2 f_{\mathrm{B}}\, d\boldsymbol{\zeta} + \mathbb{R}\mathbb{T}\rho = -\mathbb{R}\mathbb{T}(\sqrt{2}a_5 - \tfrac{a_2^2}{a_0}), \\
\sigma_{12} &= -\int_{-\infty}^{+\infty} (\zeta_1 - u)(\zeta_2 - v) f_{\mathrm{B}}\, d\boldsymbol{\zeta} + \mathbb{R}\mathbb{T}\rho = -\mathbb{R}\mathbb{T}(a_3 - \tfrac{a_1 a_2}{a_0}),
\end{aligned}
\tag{13}
$$

and the reverse

$$
a_0 = \rho,\ a_1 = \tfrac{u\rho}{\sqrt{\mathbb{R}\mathbb{T}}},\ a_2 = \tfrac{v\rho}{\sqrt{\mathbb{R}\mathbb{T}}}, \tag{14}
$$

$$
a_3 = \tfrac{uv\rho - \sigma_{12}}{\sqrt{\mathbb{R}\mathbb{T}}},\ a_4 = \tfrac{\sqrt{2}}{2}\tfrac{u^2\rho - \sigma_{11}}{\sqrt{\mathbb{R}\mathbb{T}}},\ a_5 = \tfrac{\sqrt{2}}{2}\tfrac{v^2\rho - \sigma_{22}}{\sqrt{\mathbb{R}\mathbb{T}}}. \tag{15}
$$

3.2 Recovering the Navier-Stokes equations

Following [3], we can recover the Navier-Stokes equations from (10) under the condition that the relaxation time (or the mean free path) and the Mach number goes to zero, i.e., the model is valid only in the weakly compressible case. Let us denote γ, $\mathit{\Gamma}_0$, $\mathit{\Gamma}_1$ as three time scales with the relation $\gamma \ll \mathit{\Gamma}_0 \ll \mathit{\Gamma}_1$. Here γ is of the order of the collision time, $\mathit{\Gamma}_0$ is an intermediate time scale, small enough to consider the values of the macroscopic quantities to be independent of time, and $\mathit{\Gamma}_1$ is the macroscopic time scale on which changes in the density and momentum appears. The coefficients (a_0, a_1, a_2), can be considered to be independent of time on the scale $\mathit{\Gamma}_0$ under the condition that γ is very small, i.e., in the highly collisional regime. Meanwhile, we obtain the relation between the stresses and the flow field through a kinematic viscosity $\nu = \mathbb{R}\mathbb{T}\gamma$ and the equation of state $p = \mathbb{R}\mathbb{T}\rho$. The coefficients ($a_3$, a_4, a_5) are related to the macroscopic variables as

$$
\begin{aligned}
a_3 &= -\gamma(\tfrac{\partial \rho v}{\partial x_1} + \tfrac{\partial \rho u}{\partial x_2}) + \tfrac{uv\rho}{\mathbb{R}\mathbb{T}}, \\
a_4 &= -\gamma\sqrt{2}\tfrac{\partial \rho u}{\partial x_1} + \tfrac{u^2\rho}{\sqrt{2}\mathbb{R}\mathbb{T}}, \\
a_5 &= -\gamma\sqrt{2}\tfrac{\partial \rho v}{\partial x_2} + \tfrac{v^2\rho}{\sqrt{2}\mathbb{R}\mathbb{T}}.
\end{aligned}
\tag{16}
$$

Substituting (14) and (16) into the first three equations in (10), one recovers

$$\begin{aligned}
&\tfrac{\partial \rho}{\partial t} + \tfrac{\partial \rho u}{\partial x_1} + \tfrac{\partial \rho v}{\partial x_2} = 0, \\
&\tfrac{\partial \rho u}{\partial t} + \tfrac{\partial \rho u^2}{\partial x_1} + \tfrac{\partial \rho uv}{\partial x_2} + \tfrac{\partial p}{\partial x_1} = \tfrac{\partial \sigma_{11}}{\partial x_1} + \tfrac{\partial \sigma_{12}}{\partial x_2}, \\
&\tfrac{\partial \rho v}{\partial t} + \tfrac{\partial \rho uv}{\partial x_1} + \tfrac{\partial \rho v^2}{\partial x_2} + \tfrac{\partial p}{\partial x_2} = \tfrac{\partial \sigma_{12}}{\partial x_1} + \tfrac{\partial \sigma_{22}}{\partial x_2}, \\
&\sigma_{\alpha\beta} = \mathbb{R}\mathbb{T}\gamma(\tfrac{\partial \rho u_\alpha}{\partial x_\beta} + \tfrac{\partial \rho u_\beta}{\partial x_\alpha}),
\end{aligned} \tag{17}$$

which we recognize as the isentropic compressible Navier-Stokes equation, (1), in the limit of $\nabla \cdot \boldsymbol{u} \simeq 0$, i.e., the weakly compressible limit. We refer to [3,5] for further aspects of this approximation.

3.3 Numerical examples

To validate the performance of the BGK approximation derived above as an approximation to the full Navier-Stokes equations, let us in the following consider a few examples of a more classic nature. Throughout we assume $\mathbb{R}\mathbb{T} = 1$.

The equations themselves are solved using a discontinuous Galerkin methods in space with a 4th order Runge-Kutta method in time. While the details of such a scheme can be derived from [6], we shall not discuss them further here since they are less important. Any reasonable and accurate computational techniques can be used to numerically solve (11).

3.3.1 Combined Couette-Poiseuille flow between plates

In [5] a simple Poiseuille flow was consider as a benchmark with good success. Let us consider a slightly more complicated case, the combined Coutte-Poiseuille flow between parallel plates, which is a Couette flow being driven by a constant pressure gradient in addition to the moving upper wall. The exact steady laminar solution with no-slip boundary conditions $\boldsymbol{u}(\pm h) = 0$ is

$$\frac{u}{U} = \frac{1}{2}(1 + \frac{y}{h}) + P(1 - \frac{y^2}{h^2}), \qquad P = (-\frac{dp}{dx})\frac{h^2}{2\nu U}, \tag{18}$$

where U is the velocity of the moving top wall. P is determined by the constant pressure gradient once other parameters are fixed. Fig. 1 illustrates the computational mesh and parameters employed in the combined Couette-Poiseuille flow.

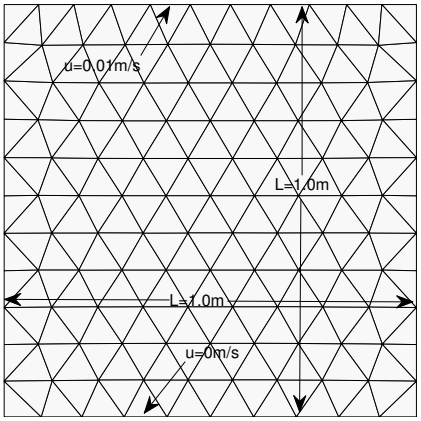

Fig. 1 Mesh and boundary conditions for the combined Couette-Poiseuille flow.

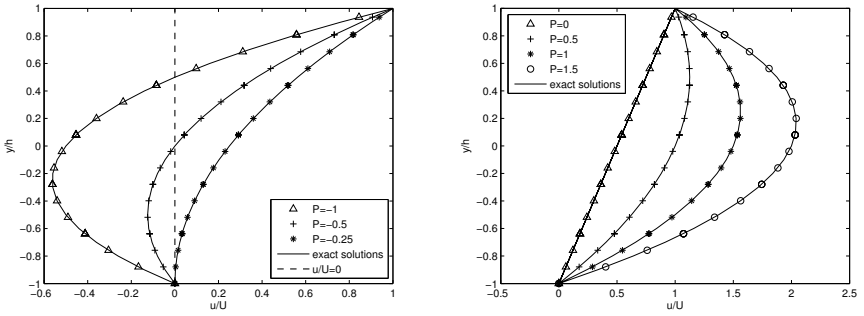

Fig. 2 $\nu = 0.01m^2/s$, symbols and lines are the normalized numerical solutions and the exact solutions respectively, Left: $P < 0$, Right: $P \geq 0$.

Fig. 2 shows that the normalized numerical solutions agree well with the exact solutions for various values of the back pressure. In agreement with previous related work in [5], convergence studies confirms the accuracy of the computational scheme, exhibiting spectral convergence for the simple problems considered here.

3.3.2 Lid-driven cavity flow

As a more challenging problem, let us consider the classic lid-driven cavity flow. It has been studied extensively by many researchers for more than three decades.

One difficulty associated with the driven cavity flow is the presence of pressure singularities at the two corners, impacting the smoothness and accuracy of the solution in the neighborhood of these. Using a standard approach, often refereed to as the regularized driven cavity [1], we assume that the velocity of the upper wall of the cavity is defined as

$$u(x) = \begin{cases} c_1x^4 + c_2x^3 + c_3x^2 + c_4x^1, & 0 \le x < 0.2, \\ 1, & 0.2 \le x \le 0.8, \\ d_1x^4 + d_2x^3 + d_3x^2 + d_4x^1 + d_5, & 0.8 < x \le 1. \end{cases} \tag{19}$$

where $[c_1, c_2, c_3, c_4] = 10^3 * [4.9333, -1.4267, 0.1297, -0.0033]$ and $[d_1, d_2, d_3, d_4, d_5] = 10^4 * [0.4933, -1.8307, 2.5450, -1.5709, 0.3633]$. In Fig. 3 we illustrate the description of the boundary conditions and the shape of regularized velocity of the lid. We use the results published in [7,8,9] to validate the computational

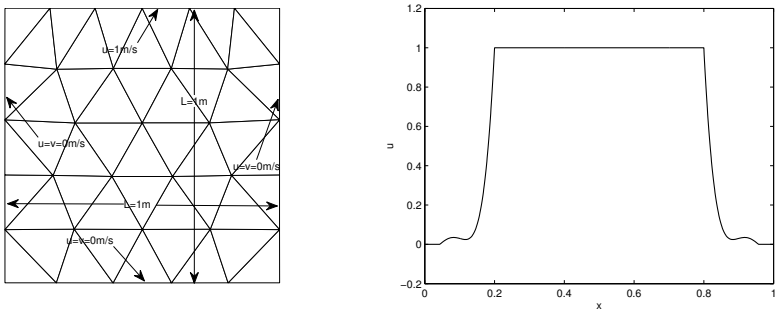

Fig. 3 Left: mesh and boundary conditions for the lid-driven cavity flow, Right: Shape of smooth driving velocity along the moving lid.

results and the physical validity of the BGK approximation considered here. Fig. 4 shows that the BGK approximation does a surprising good job at re-

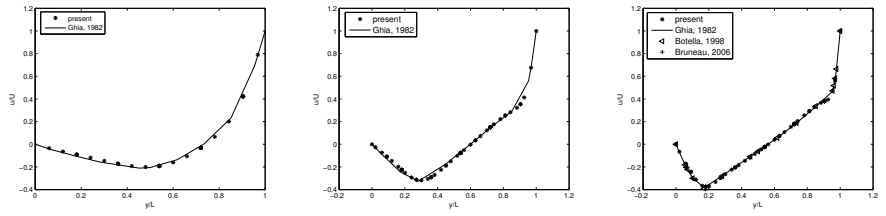

Fig. 4 Figures show the computed u-velocity along vertical line through center of cavity, compared with the existing numerical results [7, 8, 9] and the computed velocity fields. Left: Re=100, Middle: Re=400, Right: Re=1000.

producing high-quality numerical results, obtained with the full Navier-Stokes equations, this yields confidence in the validity of the model even for complex flows.

4 An absorbing layer for the BGK model

With the surprisingly good accuracy of the very simple BGK model introduced above, it is worth developing this model further, certainly as a qualitatively correct model for fluid flows with applications in e.g. computer generated imagery based on physically realistic models. One of the first questions that naturally arise when attempting to model external flows is how to best truncate the computational domain in such a way that no artificial reflections are introduced. This question is of generic and substantial importance and there is a rich literature on methods that attempts to do this, see e.g. [10, 11, 12, 13, 14, 15, 16, 17, 18, 19, 20]. While some of these methods have matured, they are still approximate and often require that only simple flows, e.g., an almost steady stream, enters into them. For more complex flows, e.g., bluff body flows with strong vortical regions, it is often required that the absorbing layers are at a substantial distance to avoid disturbances to be reflected back into the flow, disturbing the overall dynamics.

The difficulty associated with the development of efficient and robust means by which to truncate the computational domain for the compressible Navier-

Stokes equations is caused by the inherent nonlinearity of the equations. For linear hyperbolic problems such as Maxwell's equations or the equations of linear acoustics, the situation is very different. Among several alternatives, the perfectly matched layer (PML) methods, first proposed by Berenger in [21] for Maxwell's equations, offers a systematic and accurate approach of deriving absorbing layers with the attractive feature that such layers can be shown to absorb all incoming waves without any reflections, regardless of their angle of incidence or their frequency.

Observing that (11) is indeed symmetric hyperbolic it is tempting to pursue the development of a PML layer for this set of equations, hoping that such a layer could serve as an efficient and accurate way of truncating the BGK model. To derive this layer model, we shall follow the developments in [13], based on the modal analysis in Laplace-Fourier space such that solutions inside the layer decay exponentially as they propagate. However, this approach is possible only for linear low-order terms and we recall that (11) has a nonlinear low order term. Among several alternative ways of dealing with this, we pursue in this work the simplest approach in which we construct a PML for the homogeneous part of (11) only and then append the nonlinear source terms.

Without loss of generality, let us consider the construction of a PML parallel with the x_2-axis starting with $x_1 = 0$ first. Performing the Laplace transformation in time and the Fourier transformation in the x_2, the modal solution is

$$\hat{v} = e^{\lambda x_1}\hat{\Phi}(s, ik_2), \quad (-sI + \lambda A_1 + ik_2 A_2)\hat{\Phi}(x_1, ik_2) = 0. \tag{20}$$

Inside the layer, the governing equations are constructed based on the ansatz for the modal solution

$$v_L = e^{\lambda x_1 + \left[\frac{(\lambda-\lambda_1 ik_2+\lambda_0\alpha_0)}{s+\alpha_1 ik_2+\alpha_0} - \lambda_0\right]\int_0^{x_1}\sigma_1(z)dz}\hat{\Phi}(s, ik_2), \tag{21}$$

where $\lambda_0, \lambda_1, \alpha_0, \alpha_1$ are parameters that must be chosen to control behavior of the absorbing layer and (λ, Φ) are the eigensolutions of (20). Here $\sigma_1 \geq 0$ is the damping functions, assumed to be smooth and equal to zero at the interface $x_1 = 0$. In general we assume it is on the form

$$\sigma(x) = C\left(\frac{x - x_0}{L}\right)^p, \tag{22}$$

where x_0 represents the beginning of the layer of thickness L, and p is used to control the smoothness of the absorption profile. The constant C is used to control the overall strength of the absorption and generally $C \simeq (\Delta t)^{-1}$ to avoid restrictions on the explicit time step caused by the PML layer. We use the same model in all layers.

Following the approach in [17] it is straightforward to show that the PML model for the homogeneous part of Eq. (11) can be derived as

$$\begin{aligned}
&\frac{\partial \boldsymbol{a}}{\partial t} + A_1\left(\frac{\partial \boldsymbol{a}}{\partial x_1} + \sigma_1(\lambda_0 \boldsymbol{a} + \boldsymbol{\omega})\right) + A_2\left(\frac{\partial \boldsymbol{a}}{\partial x_2} + \sigma_2(\lambda_0 \boldsymbol{a} + \boldsymbol{\theta})\right) = 0\\
&\frac{\partial \boldsymbol{\omega}}{\partial t} + \alpha_1 \frac{\partial \boldsymbol{\omega}}{\partial x_2} + (\alpha_0 + \sigma_1)\boldsymbol{\omega} + \frac{\partial \boldsymbol{a}}{\partial x_1} + \lambda_0(\alpha_0 + \sigma_1)\boldsymbol{a} - \lambda_1 \frac{\partial \boldsymbol{a}}{\partial x_2} = 0,\\
&\frac{\partial \boldsymbol{\theta}}{\partial t} + \tilde{\alpha}_1 \frac{\partial \boldsymbol{\theta}}{\partial x_1} + (\tilde{\alpha}_0 + \sigma_2)\boldsymbol{\theta} + \frac{\partial \boldsymbol{a}}{\partial x_2} + \tilde{\lambda}_0(\tilde{\alpha}_0 + \sigma_2)\boldsymbol{a} - \tilde{\lambda}_1 \frac{\partial \boldsymbol{a}}{\partial x_1} = 0.
\end{aligned} \tag{23}$$

where $\boldsymbol{\omega} = (\omega_0, \omega_1, \omega_2, \omega_3, \omega_4, 0)$, $\boldsymbol{\theta} = (\theta_0, \theta_1, \theta_2, \theta_3, 0, \theta_5)$. We recall that $\sigma_i = \sigma_i(x_i)$ which suppressed for clarity.

Combing this with the nonlinear source term yields the full absorbing layer formulation for (11) as

$$\begin{aligned}
&\frac{\partial a_0}{\partial t} + \sqrt{\mathbb{RT}}\left(\frac{\partial a_1}{\partial x_1} + \frac{\partial a_2}{\partial x_2}\right) + \sqrt{\mathbb{RT}}\sigma_1(\lambda_0 a_1 + \omega_1)\\
&\quad + \sqrt{\mathbb{RT}}\sigma_2(\tilde{\lambda}_0 a_2 + \theta_3) = 0\\
&\frac{\partial a_1}{\partial t} + \sqrt{\mathbb{RT}}\left(\frac{\partial a_0}{\partial x_1} + \sqrt{2}\frac{\partial a_4}{\partial x_1} + \frac{\partial a_3}{\partial x_2}\right) + \sqrt{\mathbb{RT}}\sigma_1[\lambda_0(a_0 + \sqrt{2}a_4)\\
&\quad + (\omega_0 + \sqrt{2}\omega_4)] + \sqrt{\mathbb{RT}}\sigma_2(\tilde{\lambda}_0 a_3 + \theta_3) = 0\\
&\frac{\partial a_2}{\partial t} + \sqrt{\mathbb{RT}}\left(\frac{\partial a_3}{\partial x_1} + \frac{\partial a_0}{\partial x_2} + \sqrt{2}\frac{\partial a_5}{\partial x_2}\right) + \sqrt{\mathbb{RT}}\sigma_1(\lambda_0 a_3 + \omega_3)\\
&\quad + \sqrt{\mathbb{RT}}\sigma_2[\tilde{\lambda}_0(a_0 + \sqrt{2}a_5) + (\theta_0 + \sqrt{2}\theta_5)] = 0\\
&\frac{\partial a_3}{\partial t} + \sqrt{\mathbb{RT}}\left(\frac{\partial a_2}{\partial x_1} + \frac{\partial a_1}{\partial x_2}\right) + \sqrt{\mathbb{RT}}\sigma_1(\lambda_0 a_2 + \omega_2)\\
&\quad + \sqrt{\mathbb{RT}}\sigma_2(\tilde{\lambda}_0 a_1 + \theta_1) = -\tfrac{1}{\gamma}\left(a_3 - \tfrac{a_1 a_2}{a_0}\right)\\
&\frac{\partial a_4}{\partial t} + \sqrt{2\mathbb{RT}}\frac{\partial a_1}{\partial x_1} + \sqrt{2\mathbb{RT}}\sigma_1(\lambda_0 a_1 + \omega_1) = -\tfrac{1}{\gamma}\left(a_4 - \tfrac{a_1^2}{\sqrt{2}a_0}\right)\\
&\frac{\partial a_5}{\partial t} + \sqrt{2\mathbb{RT}}\frac{\partial a_2}{\partial x_2} + \sqrt{2\mathbb{RT}}\sigma_2(\tilde{\lambda}_0 a_2 + \theta_2) = -\tfrac{1}{\gamma}\left(a_5 - \tfrac{a_2^2}{\sqrt{2}a_0}\right),
\end{aligned} \tag{24}$$

which should be coupled with (23) for evolution of the auxiliary variables $\boldsymbol{\omega}$ and $\boldsymbol{\theta}$. The last step left is to choose parameters making solutions in the layer

damping. This leaves substantial room for optimization which we have not pursued in this work. In what follows, the parameters are assumed as follows

$$\begin{aligned} &\lambda_1 = 0,\, \lambda_0 = 0,\, \alpha_1 = 0,\, \alpha_0 \neq 0, \\ &\tilde{\lambda}_1 = 0,\, \tilde{\lambda}_0 = 0,\, \tilde{\alpha}_1 = 0,\, \tilde{\alpha}_0 \neq 0. \end{aligned} \tag{25}$$

4.1 Long time stability of absorbing layer

As was discussed at length in [10], many standard PML formulations suffer from a weak instability that will manifest itself late in certain types of applications. Let us in the following consider this question for the absorbing layer proposed in the above.

We begin by substituting (25) into (24), to obtain

$$\begin{aligned} &\frac{\partial \boldsymbol{a}}{\partial t} + A_1\left(\frac{\partial \boldsymbol{a}}{\partial x_1} + \sigma_1 \boldsymbol{\omega}\right) + A_2\left(\frac{\partial \boldsymbol{a}}{\partial x_2} + \boldsymbol{\theta}\right) = S(\boldsymbol{a}) \\ &\frac{\partial \boldsymbol{\omega}}{\partial t} + (\alpha_0 + \sigma_1)\boldsymbol{\omega} + \frac{\partial \boldsymbol{a}}{\partial x_1} = 0, \\ &\frac{\partial \boldsymbol{\theta}}{\partial t} + (\tilde{\alpha}_0 + \sigma_2)\boldsymbol{\theta} + \frac{\partial \boldsymbol{a}}{\partial x_2} = 0. \end{aligned} \tag{26}$$

To continue, we follow [10] and assume that the absorbing layer is almost quiescent, i.e., we assume all spatial derivates are very small. This allows us to divide (26) into three parts, in which the first part is

$$\begin{aligned} &\frac{\partial \boldsymbol{\omega}}{\partial t} + (\alpha_0 + \sigma_1)\boldsymbol{\omega} = 0, \\ &\frac{\partial \boldsymbol{\theta}}{\partial t} + (\tilde{\alpha}_0 + \sigma_2)\boldsymbol{\theta} = 0, \end{aligned} \tag{27}$$

for which, in the simplest case of assuming $\sigma_i \geq 0$ but constant, one easily recovers the analytic solutions as

$$\boldsymbol{\omega} = e^{-(\alpha_0+\sigma_1)t}\boldsymbol{\omega}(0), \qquad \boldsymbol{\theta} = e^{-(\tilde{\alpha}_0+\sigma_2)t}\boldsymbol{\theta}(0), \tag{28}$$

where $\boldsymbol{\omega}(0)$ and $\boldsymbol{\theta}(0)$ are the initial conditions which are typically assumed to be very small or zero.

The second part is

$$\begin{aligned} &\frac{\partial a_0}{\partial t} + \sqrt{\mathbb{R}\mathbb{T}}\sigma_1\omega_1 + \sqrt{\mathbb{R}\mathbb{T}}\sigma_2\theta_2 = 0, \\ &\frac{\partial a_1}{\partial t} + \sqrt{\mathbb{R}\mathbb{T}}\sigma_1(\omega_0 + \sqrt{2}\omega_4) + \sqrt{\mathbb{R}\mathbb{T}}\sigma_2\theta_3 = 0, \\ &\frac{\partial a_2}{\partial t} + \sqrt{\mathbb{R}\mathbb{T}}\sigma_1\omega_3 + \sqrt{\mathbb{R}\mathbb{T}}\sigma_2(\theta_0 + \sqrt{2}\theta_5) = 0, \end{aligned} \tag{29}$$

With the three equations being decoupled and the strictly decaying nature of $\boldsymbol{\omega}$ and $\boldsymbol{\theta}$ it is clear that also (a_0, a_1, a_2) will approximate to a constant.

The final part is given as

$$\begin{aligned}
\tfrac{\partial a_3}{\partial t} &+ \sqrt{\mathbb{RT}}\sigma_1\omega_2 + \sqrt{\mathbb{RT}}\sigma_2\theta_1 = -\tfrac{1}{\gamma}(a_3 - \tfrac{a_1 a_2}{a_0}),\\
\tfrac{\partial a_4}{\partial t} &+ \sqrt{2\mathbb{RT}}\sigma_1\omega_1 = -\tfrac{1}{\gamma}(a_4 - \tfrac{a_1^2}{\sqrt{2}a_0}),\\
\tfrac{\partial a_5}{\partial t} &+ \sqrt{2\mathbb{RT}}\sigma_2\theta_2 = -\tfrac{1}{\gamma}(a_5 - \tfrac{a_2^2}{\sqrt{2}a_0}),
\end{aligned} \tag{30}$$

Considering the long time limit in which the auxiliary variables vanishes and (a_0, a_1, a_2) approaches a constant, the equations for each of the three variables take the form

$$\frac{\partial a_i}{\partial t} = -\frac{1}{\gamma}a_i + b,$$

where b represents the asymptotic limit of the three nonlinear terms. It is clear that if $\gamma > 0$, $a_i(t)$ will decay to zero. Since γ is a measure of collision time, positivity is guaranteed and, hence, long time stability of the layer is established.

4.2 Numerical evaluation of absorbing layer

With the derivation of the absorbing layer model above, it is natural to consider in a more careful manner the performance of this layer for various test cases. Hence, we will continue to solve the BGK-related model but now add the absorbing layer to enable the modeling of open problems.

4.2.1 Acoustic wave

In this section, we consider a case where a simple acoustic wave is generated in the center of computational domain, composed by the square $(x_1, x_2) \in [-2, 2]^2$, surrounded by a layer of thickness L with the outer layer terminated by characteristic boundary conditions. As an exact solution we consider the numerical solution obtained in the domain $[-10, 10]^2$ and terminate the solution before reflections can reach the computation domain. This is done to

isolate errors caused by the absorbing layers only and eliminate other sources of numerical errors in the comparison.

The initial conditions are given as

$$\rho(\boldsymbol{x},0) = 1 + \exp\left(-\frac{|\boldsymbol{x}-\boldsymbol{c}|^2}{b}\right), \quad u = v = 0,$$

with $\boldsymbol{c} = (0.1, 0.1)$ and $b = 0.1$. In the absorbing layer we use $C = 120$ in (22) and $\alpha_0 = 10$, $\tilde{\alpha}_0 = 10$. These parameters remain unchanged unless stated otherwise.

In Fig. 5 we illustrate the behavior of the absorbing layers for increasing value of width of the layer and smoothness of the absorption profile. The results indicate an initial phase where the characteristic boundary conditions appear to be superior. This is, however, an artifact of the computational setup in which the characteristic boundary is placed at a distance equivalent to that including the width of the absorbing layer. Hence, when compared with the absorbing layer results, there is a longer period of time where no refections can reach the point of measurement, resulting in errors that reflect approximation error rather than reflections due to the termination of the computational domain. For longer periods of time, however, the absorbing layer is superior to the characteristic boundary conditions and shows the expected improvement in accuracy as the width of the layer increases while a decay in accuracy for increasing smoothness. The results are obtained in a specify point, $(1, 1)$, but similar results and qualitative behavior is observed in other points. As discussed previously, it is conceivable that different choices of the parameters in the absorbing layer can be adjusted to improve the performance.

4.3 Uniform flow past a circular cylinder

As a more complex case, we consider the classic von Karman problem of a viscous compressible uniform flow past a circular cylinder of diameter d, in this case takes to be 0.2, and the computational domain in $(x_1, x_2) \in [-1, 2] \times [-1, 1]$.

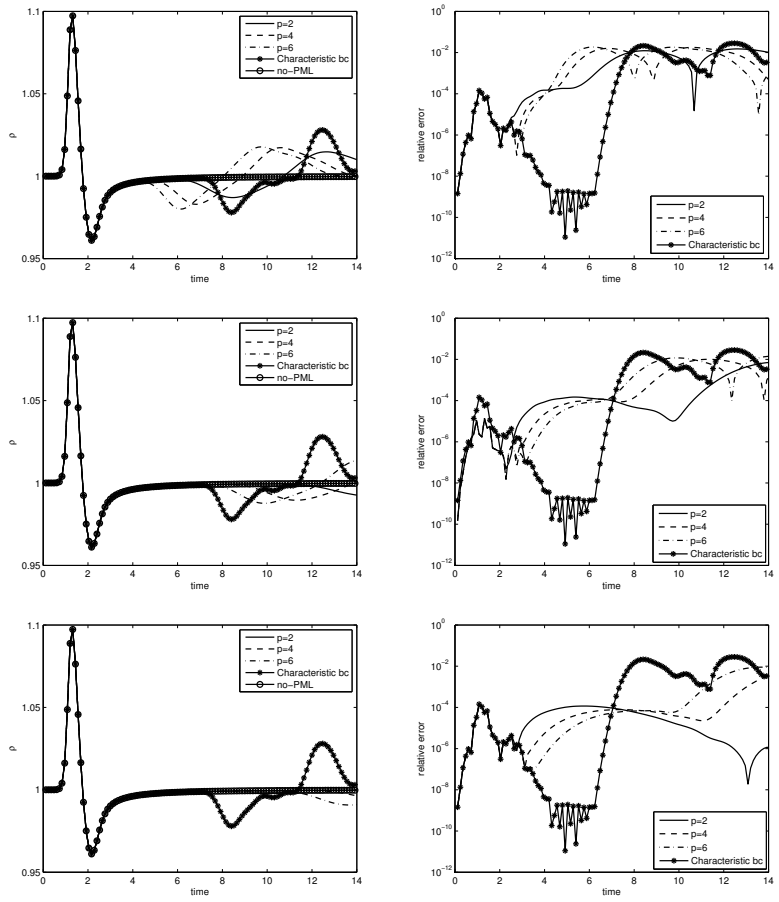

Fig. 5 Left column shows the computed density at point (1,1) for increasing width of the layer, $L = 1, 2, 3$ for the three rows. The actual pointwise error is shown in the second column.

The initial conditions in all test cases are given as

$$\rho_0 = 1, \qquad u_0 = 0.5, \qquad v_0 = 0. \tag{31}$$

It is standard to define Reynolds number as

$$Re = \frac{\rho u_0 d}{\nu} \tag{32}$$

where ρ_0, ν are considered as constants. The dimensionless time is defined by

$$T = \frac{u_0 t}{d}. \tag{33}$$

Above a critical Reynolds number it is well known that the flow becomes unstable and enters into a periodic shedding cycle, creating the celebrated von Karman streak. The shedding frequency is measured through the non-dimensional Strouhal number defined as

$$St = \frac{fd}{u_0}. \tag{34}$$

where f is the dimensionless frequency of the shedding of the vortices rear of the cylinder.

To validate the performance of the absorbing layer, we consider two different cases, sketched in Fig. 6. In the first test, the layer is just downstream of the cylinder and characteristic boundary conditions are used elsewhere while in the second set of tests the computational domain is entirely surrounded by the absorbing layers.

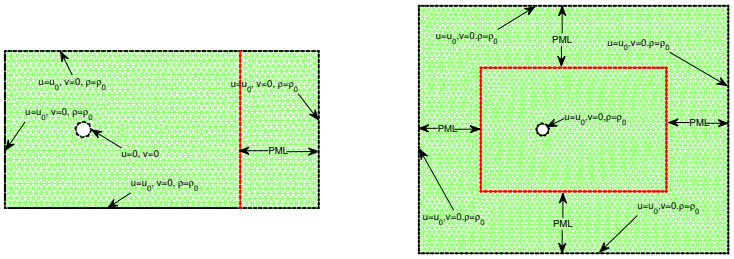

Fig. 6 Examples of meshes and boundary conditions of the computational model with one sided and four sided absorbing layers.

In the absorbing layer, we again use $C = 120$ in (22) and this time take $\alpha_0 = \tilde{\alpha}_0 = 10$. As a reference solution to directly measure reflections, we solve the problem in a larger domain, extended with 2 units in all direction.

In Fig. 7 we show a direct comparison between the results obtained by the one sided absorbing layer and reference solutions obtained in a larger

computational domain. The error is measured in the fixed point $(0.5, 0.5)$. The agreement remains excellent and confirms the accuracy of this proposed absorbing layer for uniform flow past a cylinder. For a more qualitative measure

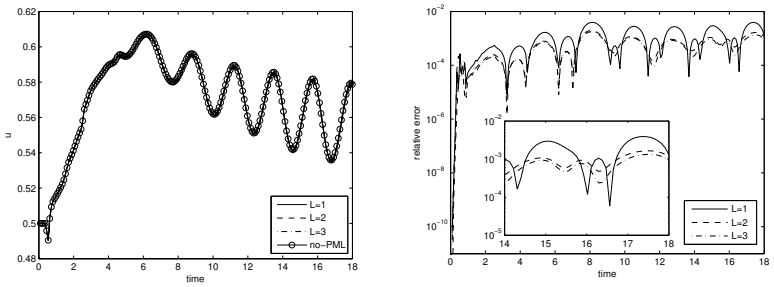

Fig. 7 Flow past a cylinder problem with a one-sided ($p = 2$) absorbing layer at $Re = 100$. On the left, we show the computed velocity u, computed with different widths of the absorbing layer and compared with the solution obtained in a larger domain. The right shows the associated relative error.

of performance, we show in Fig. 8 the development of the vortex shedding in the density and u-velocity at different times. Even a careful inspection does not reveal any adverse effect of the absorbing layer and an effective absorption of vortices down stream of the cylinder.

To further verify the accuracy and efficiency of the proposed approach, in Fig. 9 we show the direct comparison between four sides PML model with and the reference solutions. The shifts in oscillation is caused by the differences in the initial conditions and we observe that after this initial phase, frequency of the oscillations remain the same.

To validate the long time behavior, we show in Fig. 10 contour plots of both density and velocity at a late stage (T=30) where the vortex dynamics is fully developed and the layer has absorbed numerous vortices. We do not see any effects of reflections from either the single layer or the fully enclosing four sided absorbing layer, further giving confidence in the proper behavior of the proposed approach.

As a final measure of accuracy of the simulations, we shall use the Strouhal number. While there is no known exact expression for the scaling of the Stroudal number with Reynolds number, extensive experimentation has provided an empirical relation between the Strouhal number and the Reynolds number (60-180) as

$$S_t = \frac{-3.3265}{Re} + 0.1816 + 0.00016Re. \tag{35}$$

The numerical frequency in (34) are measured by taking a time series, i.e. 30 seconds of the pressure at the fixed point $(0, 1)$.

The numerical Strouhal numbers corresponding to various Reynolds numbers are shown in Fig. 11 and compared with the experimental scaling. We note that the BGK model displays the correct qualitative scaling with the Reynolds number but it is quantitative value is incorrect. Extensive experimentation suggests that this is caused by the simplicity of the model which proves inadequate when attempting to model the complex boundary layer dynamics giving rise to the vortex shedding. However, the quality and accuracy of the proposed absorbing layer remains unchallenged after these tests.

5 Terminating the Navier-Stokes equations with the BGK-based absorbing layer

Having realized the limitations of the BGK model to provide quantitatively correct results, albeit the results are clearly of qualitative value, it is worth considering ways to take advantage of the developed absorbing layer model as an approach to truncate the computational domain when solving the more accurate compressible Navier-Stokes equations.

We pursue this by considering an approach where we solve the fully compressible Navier-Stokes equations (1) using a discontinuous Galerkin method, discussed at length in [6]. While this is not an essential choice, the locality of this particular flux-based method makes it possible to couple the physically correct Navier-Stokes equations, solved in the computational domain, with the qualitatively correct BGK approximation in adjacent domains. Hence, one

can simply use the direct relation between the BGK variables and the physical variables (13)-(15) to relate the solutions in the two neighboring parts of the domain and connect them through the numerical flux. This is a simple and straightforward approach that lends itself to a direct implementation in a discontinuous Galerkin or finite volume formulation.

With this approach is mind, it is natural to consider truncating the compressible Navier-Stokes equations with absorbing layers base on a BGK-based approach discussed above, i.e., one solves the compressible Navier-Stokes equations in the computation domain of interest but truncates the computational domain with the BGK-model modified to allow only decaying solutions, hence having achieved the formulation on an absorbing layer for the compressible Navier-Stokes equations.

Let us in the following revisit the two test cases we considered for the pure BGK-approximation to evaluate this multi-model approach to the development of an efficient and stable absorbing layer for the full Navier-Stokes equations.

5.1 Acoustic wave

We consider a case where a simple acoustic wave is generated in the center of computational domain, composed by the square $(x_1, x_2) \in [-2, 2]^2$ in which (1) is solved, surrounded by a BGK-layer of thickness L with the outer layer terminated by characteristic boundary conditions. As an exact solution we consider the numerical solution of the full Navier-Stokes equations obtained in the domain $[-10, 10]^2$ and terminate the solution before reflections can reach the computation domain.

The initial conditions are given as

$$\rho(\boldsymbol{x}, 0) = 1 + \exp\left(-\frac{|\boldsymbol{x} - \boldsymbol{c}|^2}{b}\right), \quad u = v = 0,$$

with $\boldsymbol{c} = (0.1, 0.1)$ and $b = 0.1$. In the absorbing layer we use $C = 120$ in (22) and $\alpha_0 = 10$, $\tilde{\alpha}_0 = 10$. These parameters remain unchanged unless stated otherwise.

In Fig. 12 we illustrate the behavior of the absorbing layers for increasing value of width of the layer and smoothness of the absorption profile. Even though the model is now considerably more complex, the overall behavior is as one would expect based on the previous tests and the results show the expected improvement in accuracy as the width of the layer increases while a decay in accuracy for increasing smoothness. The results are obtained in a specific point, $(1, 1)$, but similar results and qualitative behavior is observed in other points. In Fig. 12 we also show the results obtained with a $L = 4$ thick layer in which case the accuracy is clearly superior to what is possible with the characteristic boundary condition.

5.2 Uniform flow past a circular cylinder

As the second and more complex case, we again consider the classic von Karman problem of a viscous compressible uniform flow past a circular cylinder of diameter d, in this case takes to be 0.2, and the computational domain in $(x_1, x_2) \in [-1, 2] \times [-1, 1]$. As in the previous case, we take the initial conditions to be

$$\rho_0 = 1, \qquad u_0 = 0.5, \qquad v_0 = 0. \tag{36}$$

For an initial qualitative measure of performance, we show in Fig. 13 the development of the vortex shedding in the density and u-velocity at different points in time. Even a careful inspection does not reveal any adverse effect of the absorbing layer and an effective absorption of vortices down stream of the cylinder. Similar results are obtained in the case where the computational domain is entirely surrounded by the BGK-based absorbing later.

As a more quantitative measure of performance we show in Fig. 14 the time-averaged pressure at two different values of the Reynolds number and compared with the results of a much more extensive computation involving the solution of the full Navier-Stokes equations in a larger domain. Even a careful inspection reveals that the differences are minimal and there are no

visible disturbances or reflections caused by the absorbing layer in spite of it being placed at a downstream distance of less than 7 cylinder diameters.

As a final test, we again compute the scaling of the Stroudal number with Reynolds number, shown in Fig. 15. As one would expect the scaling is now correct and in agreement with experimental predictions.

6 Concluding Remarks

This work contains several apparently different directions of inquiry that are ultimately combined to present a new approach to the development of accurate absorbing layers to the compressible Navier-Stokes equations in the low Mach number regime. By taking a detour and evaluating the accuracy of a relatively crude approximation of the Navier-Stokes equations, arrived at by considering the Boltzman equation with a BGK-collision term, we demonstrated the potential for deriving an efficient absorbing layer for BGK model. The crucial issue here is that the approximation to the BGK model has a linear principal part and we explored this to develop an absorbing layer using general results for perfectly matched layers for linear hyperbolic systems. The resulting scheme is relatively simple and straightforward to implement and we evaluated its efficiency through a number of examples.

These examples also showed, however, that the simple BGK-approximation has limitations, in this case illustrated by bluff-body flows. To address this, and close the loop of this work, we demonstrated how the absorbing layer developed for the BGK-model could be combined with the BGK model itself to recover an absorbing layer for the compressible Navier-Stokes equations. Computational results confirms stability and accuracy of the approach and open the path to the development of a new generation of absorbing layers for compressible Navier-Stokes equations.

In this work, the emphasis has been on demonstrating this hybrid approach and many issues and parameters are open to optimization. It is conceivable that such optimization allows for substantial performance enhancements of the layers. Furthermore, the focus has been on low Mach number problems but

choosing alternative Boltzman model may well allow this to be extended to strongly compressible flows and, potential, even to problems with shocks. We hope to be able to consider some of these questions in future work.

Acknowledgement

The first author acknowledges Prof. Wai Sun, Don for useful discussion on characteristic boundary condition, also thanks Prof. Allan P. Engsig-Karup for two-dimensional codes for solving compressible Navier-Stokes equation. The second author acknowledges partial support by AFOSR, NSF, and DoE. The third author acknowledges partial support by the NSF through award DMS-0810187.

References

1. R. Peyret and T. D. Taylor, Computational Methods for Fluid Flow, Springer, New York, 1983.
2. S. Chapman, T. G. Cowling, The Mathematical Theory of Non-Uniform Gases (Cambridge University Press, 3rd edn., 1990).
3. H. Grad, On the Kinetic theory of rarefied gases, Commun. Pure Appl. Math. 2, 1949, 331-407.
4. J. P. Boyd, Chebysheve and Fourier Spectral Methods, Springer, Berlin, 1989.
5. J. Tölke, M. Krafczyk, M. Schulz, E. Rank, Discretization of the Boltzmann equation in velocity space using a Galerkin approach, Comput. Phys. Commun. 129, 2000, 91-99.
6. J. S. Hesthaven and T. Warburton, Nodal Discontinuous Galerkin Methods: Algorithms, Analysis, and Applications. Springer Verlag, New York, 2007.
7. U. Ghia, K. N. Ghia and C. T. Shin, High-resolutions for incompressible flows using Navier-Stokes equations and a multigrid method. J Comput Phys 48, 1982, 387-411.
8. O. Botella and R. Peyret, Benchmark spectral results on the lid-driven cavity flow. Comput. & Fluids 27(4), 1998, 421-433.
9. Ch-H. Bruneau and M. Saad, The 2D Lid-driven cavity problem revisited., Comput. & Fluids, 35, 2006, 326-348.
10. J. S. Hesthaven, On the analysis and construction of perfectly matched layers for the linearized Euler equations, J. Comput. Phys. 142 (1), 1998, 129-147.
11. E. Turkel, A. Yefet, Absording PML boundary Layers for wave-like equations, Appl. Numer. Math. 27 (4), 1998, 533-537. Special Issue on Absorbing Boundary Conditions.

12. S. Abarbanel, D. Stanescu and M.Y. Hussaini, Unsplit variables perfectly matched layers for the shallow water equations with Coriolis forces, Comput. Geosci. 7, 2003, 275-294.
13. T. Hagstrom, A new construction of perfectly matched layers for hyperbolic systems with applications to the linearized Euler equations, in: G. Cohen, E. Heikkola, P. Joly, P. Neittaanmäki (Eds.), Mathematical and Numerical Aspects of Wave Propagation Phenomena, Springer-Verlag, Berlin, 2003, 125-129.
14. I. M. Navon, B. Neta and M.Y. Hussaini, A perfectly matched layer approach to the linearized shallow water equations models, Monthly Weather Review, 132, 2004, 1369-1378.
15. F. Q. Hu, A perfectly matched layer absorbing boundary condition for linearized Euler equations with a non-uniform mean-flow, J. Comput. Phys. 208, 2005, 469-492.
16. D. Appelö, G. Kreiss, A new absorbing layer for elastic waves, J. Comput. Phys. 215, 2006, 642-660.
17. D. Appelö, T. Hagstrom, G. Kreiss, Perfectly matched layers for hyperbolic systems: General formulation, well-posedness and stability, SIAM J. Appl. Math. 67(1), 2006, 1-23.
18. C. Zheng, A perfectly matched layer approach to the nonlinear Schrödinger wave equations, J. Comput. Phys. 227, 2007, 537-556.
19. F. Q. Hu, X. D. Li and D. K. Lin, Absorbing boundary conditions for nonlinear Euler and Navier-Stokes equations based on the perfectly matched layer technique, J. Comput. Phys. 227, 2008, 4398-4424.
20. T. Dohnal, Perfectly matched layers for coupled nonlinear Shrödinger equations with mixed derivatives, J. Comput. Phys. 228, 2009, 8752-8765.
21. J. P. Berenger, A Perfectly Matched Layer for the Absorption of Electromagnetic waves, J. Comput. Phys. 114, 1994, 185-200.

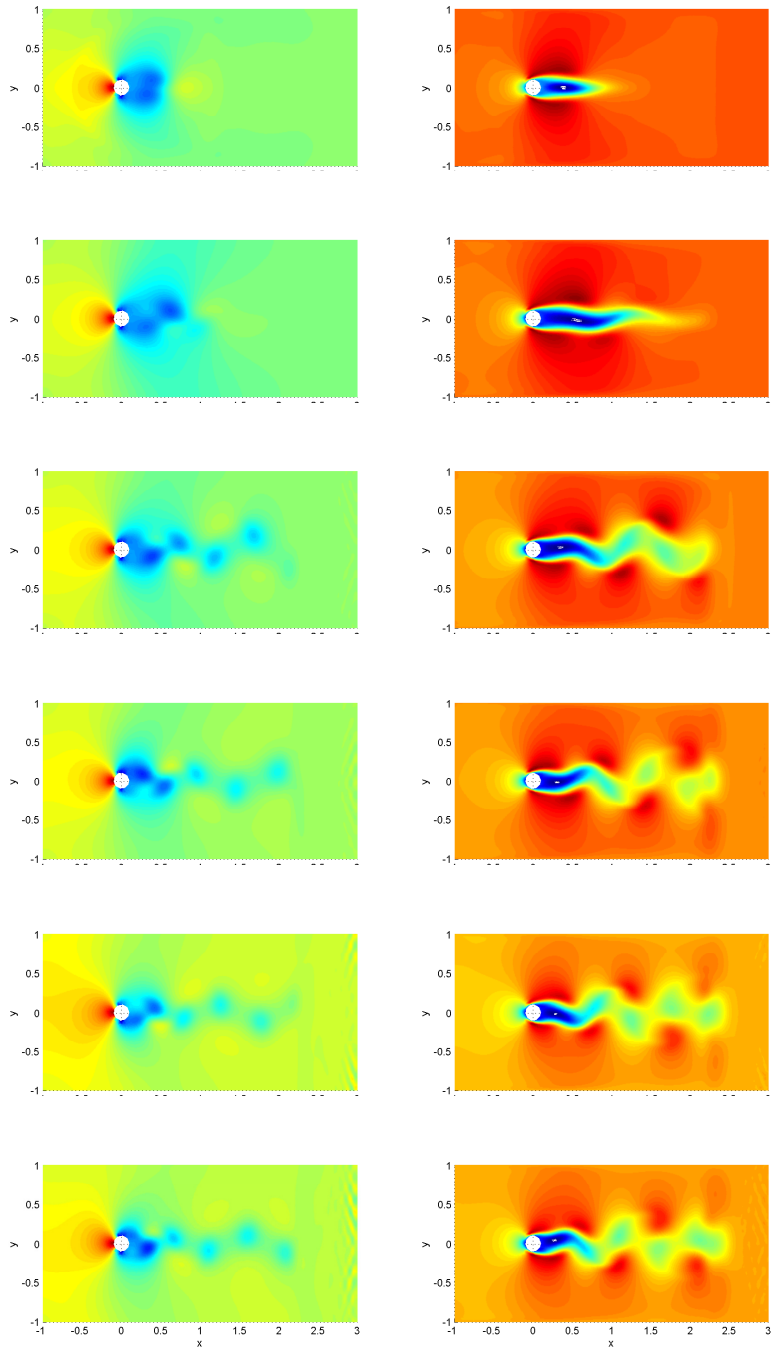

Fig. 8 Flow past a cylinder problem with a downstream absorbing layer at $Re = 100$. We show the contours of the density (left) and the u-velocity (right) at non-dimensional times of 3-18 with 3 units separation.

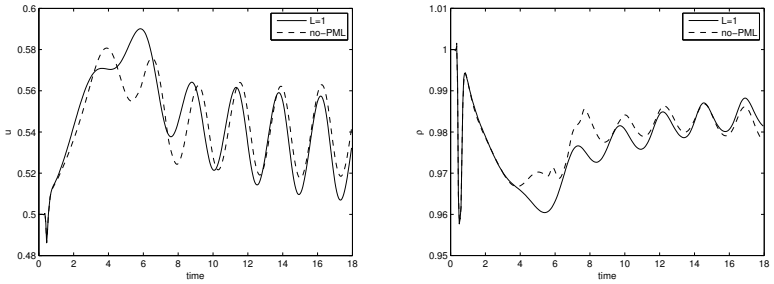

Fig. 9 Flow past a cylinder problem with four sided absorbing layer at $Re = 100$. On the left, we show the computed velocity u compared with that computed in the larger domain. The right shows the corresponding density.

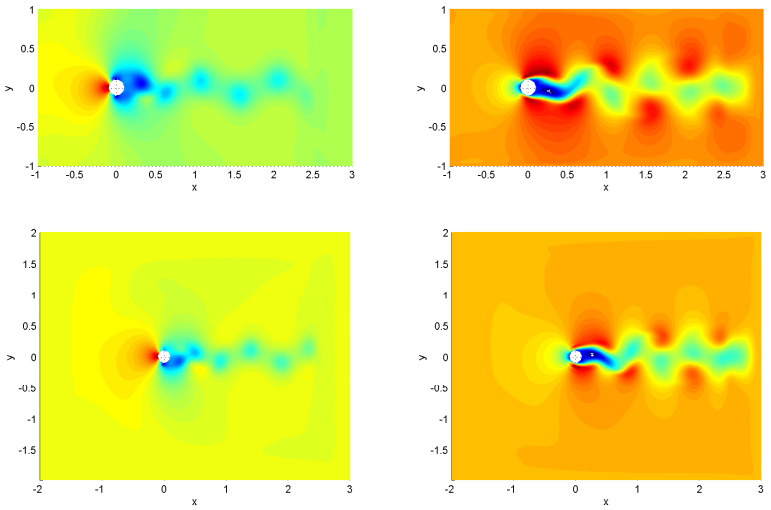

Fig. 10 Late time fully developed flow past a circular cylinder at Re=100. The figure contains results for both a single layer (top) and four layers (bottom) and we show results of both the density (left) and the u-velocity (right).

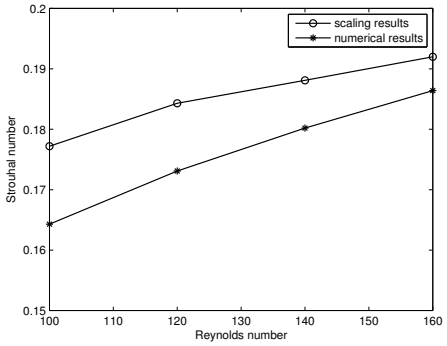

Fig. 11 Strouhal number as a funcition of the Reynolds number, computed using the BGK model and compared with an experimentally determined scaling law.

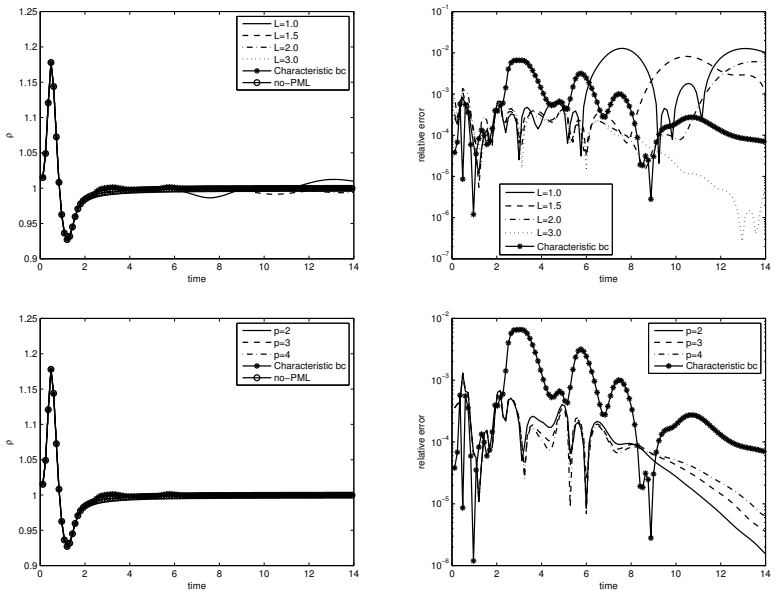

Fig. 12 Left column shows the computed density at point (1,1) for increasing width of the layer with $p = 2$ in the profile (top) as well as the density computed with $L = 4$ and increasing layer smoothness. The actual pointwise error for these two cases are shown in the second column.

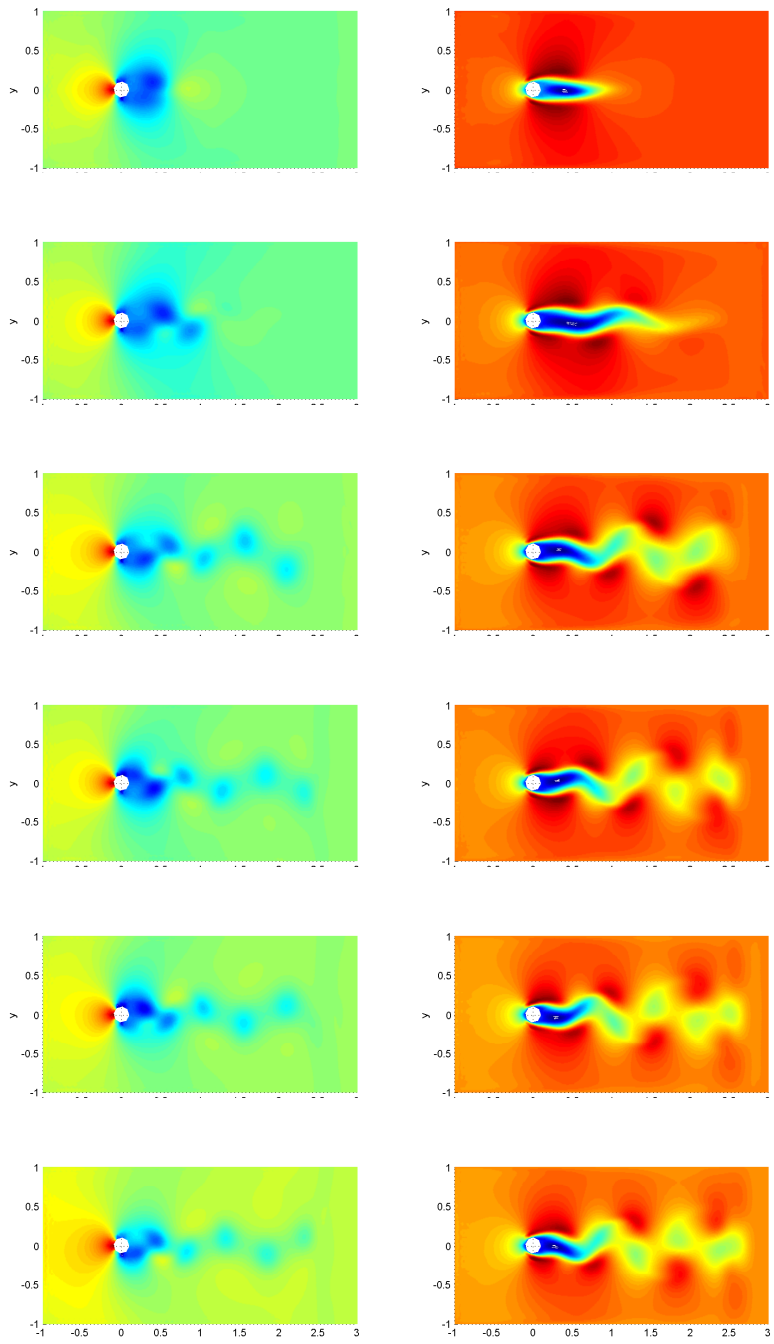

Fig. 13 Flow past a cylinder problem modeling using a compressible Navier-Stokes equations with a downstream BGK-based absorbing layer at $Re = 100$. We show the contours of the density (left) and the u-velocity (right) at non-dimensional times of 3-18 with 3 units separation.

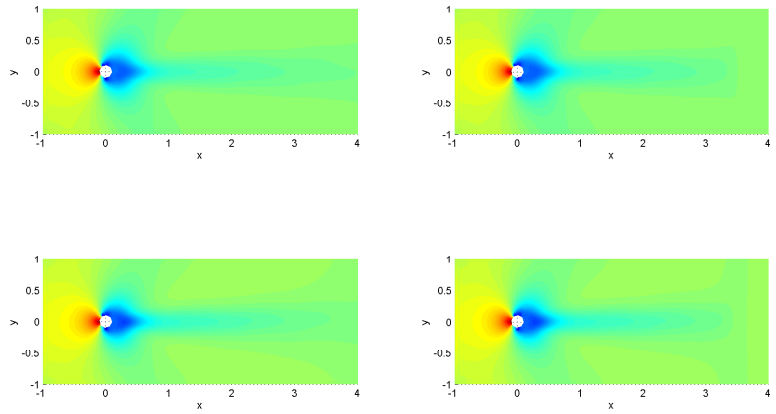

Fig. 14 Time averaged pressure field at Re=120 (top row) and Re=140 (bottom row). In the left column we show the time averaged pressure computed in a larger domain and truncated while the right column shows the average pressure computed with the BGK-based absorbing layer starting at x=3.

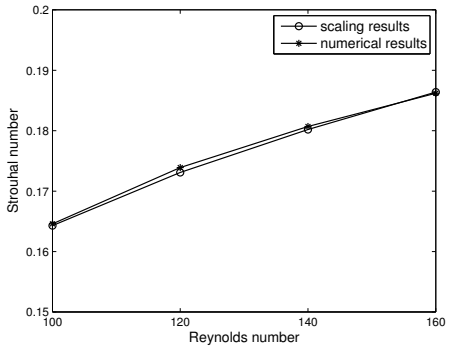

Fig. 15 Strouhal number as a funcition of the Reynolds number, computed using the full compressible Navier-Stokes model truncated with a BGK-based absorbing layer and compared with an experimentally determined scaling law.